Mycobacterial load and direct contact primes spacious to compact phagosome switching for egress

Aher Jayesh Bhausaheb[1,2], Aniruddha Nagarajan[2,4], Bommidi Jahnavi[5], Debraj Koiri[1,2], Jafarulla Shaikh[1,2], Sandeep Choubey[2,4], Varadharajan Sundaramurthy[5], Mohammed Saleem[1,2,3*]

Affiliations

[1] School of Biological Sciences, National Institute of Science Education & Research (NISER), Bhubaneshwar, India.
[2] Homi Bhabha National Institute (HBNI), Mumbai, India.
[3] Center for Interdisciplinary Sciences, National Institute of Science Education & Research (NISER), Bhubaneshwar, India.
[4]Institute of Mathematical Sciences (IMSc), Chennai, India.
[5]National Centre for Biological Sciences, Bangalore, India.

*Correspondence: Mohammed Saleem (saleem@niser.ac.in)

Abstract

Mycobacterium tuberculosis (*Mtb*) establishes intracellular niches by remodeling host membranes into either spacious or compact phagosomes, yet how direct bacterial contact within these distinct compartments facilitates bacterial egress remains unknown. Using fixed cell imaging, in vitro reconstitution of phagosome-like vesicles, and numerical simulations, we uncover that mycobacterial load and its direct contact determines phagosome fate by driving membrane bending, lipid wrapping and phase separation. Low-to-moderate load induces membrane vesiculation, generating compact phagosome-like structures. High bacterial load drives a scaffold-like architecture that primes compartments for rupture via complete lipid phase separation and changes in the membrane's bending and area stretch moduli, rendering it more deformable. Notably, physical contact synergizes with the virulence factor ESAT-6, amplifying its membrane-deforming activity to disrupt phagosomal integrity. We propose that mycobacteria actively switch spacious to compact phagosomal states by modulating host membrane mechanics—a process governed by the membrane-to-contact area ratio and proximity to lipid demixing point. These findings reveal a biophysical switch in pathogen-driven membrane remodeling, with broad implications for understanding how intracellular pathogens manipulate host membranes to survive.

Introduction

The interaction of bacteria with the cellular membrane interfaces is essential for its host entry, intracellular life as well as egress [1, 2].Such highly complex processes are driven by multiple coordinated protein or lipid-dependent noncovalent interactions[3]. Several invasive bacterial pathogens, such as *Listeria monocytogenes*, *Pseudomonas aeruginosa* are known to hijack host membrane interfaces for actin polymerization resulting in the bacterial engulfment by the host cell membrane[4, 5]. *P. aeruginosa* induces cell membrane invaginations via a lipid zipper formation by the interaction between the glycosphingolipid Gb3 and the bacterial surface lectin LecA, in addition to other cell surface receptors[6]. Clathrin and Arp2/3 complexes have been identified as the key regulator of actin polymerization for zippering pathogens such as *Listeria* and *Yersinia*[7, 8]. Likewise, *Mycobacterium tuberculosis* (*Mtb*) is known to gain entry into the host cell via passive internalization or engulfment mediated by several surface adhesion proteins[9, 10]. The *Mtb* are ejected from the host cell by generating actin-based structures called ejectosomes that are aided by autophagy machinery enabling a non-lytic mechanism [11, 12]. Our understanding of bacterial host entry has been reasonably refined in recent times and mediated by a diverse set of pathogen-specific biochemical interactions. However, the disruption of the pathogen-containing vacuolar compartment of the host cell remains an open question, particularly in the case of *Mtb*[13].

Mtb survives intracellularly by hijacking the phagosome maturation [14, 15]. ESAT-6 (6kDa early secretory antigen target), a highly immunogenic effector protein secreted by *Mtb*, is critical for the process of phagosome (also referred to as Mycobacteria containing vacuole (MCV)) rupture [16, 17]. Purified recombinant ESAT-6 is known to induce lysis of cultured macrophages through permeabilization of both the phagosome membrane as well as cell membrane upon gaining access to the cytoplasm [18-20]. Despite significant evidence that supports the direct role of ESAT-6 in phagosome lysis and virulence[21-23], a recent study reported that ESAT-6 interaction alone is not sufficient for phagosome disruption. Instead, direct bacterial physical contact is important for gross phagosomal membrane disruption [24]. *In vivo* observations also suggest that ESAT-6 required additional factors such as the lipid phthiocerol dimycocerosates (PDIMs), which are complex branched cell-wall-associated lipids known to induce sterol clustering in host membranes, eventually inducing phagosome disruption [25-30]. Interestingly, *Mycobacterium marinum* transposon mutants induce phagosome damage despite their inability to secrete ESAT-6, suggesting that ESAT-6 alone may not be sufficient for the ESX-1 virulence function [31]. Though the ability to damage the phagosomal membrane has emerged central to *Mtb* virulence, the mechanism of phagosome membrane remodelling and disruption remains poorly understood [13]. *Mtb* is known to be a non-motile bacteria, however, exhibits sliding mobility upon encountering surfaces. Very recently, motile swimming bacteria such as *E. coli* and *B. subtilis* have been shown to induce non-equilibrium membrane fluctuations [32], deformations [33] as well as conferring coupled mobility in synthetic giant vesicles encapsulating the bacteria[34]. However, the dynamics and impact of direct physical contact of a non-motile bacteria with the vacuolar compartment remain unknown to date. Understanding the implications of direct physical contact of the bacteria is not only important for vacuolar

disruption but also for a broad class of bacterial pathogens interaction with host cell membranes both during internalization as well as egress.

In this work, we developed an *in vitro* reconstitution method to dissect the mechanism of phagosome membrane remodelling induced by the direct physical contact of bacteria by encapsulating live *Mycobacterium smegmatis* (as a model opportunistic bacteria) inside a host phagosome-like compartment. Furthermore, it also enables us to delineate the role of direct physical contact in phagosome membrane remodelling from virulence factors. We capture the dynamics of bacterial direct contact as well as bacterial-load-mediated host membrane remodelling. We discover that the direct-contact of an isolated *M . smegmatis* with the encapsulating host membrane results in significant lipid wrapping, membrane bending, and local lipid phase separation at the contact site. In contrast, the spacious and compact phagosome mimic with varying bacterial load induces complete lipid phase separation of the compartment. The lipid wrapping is driven by the surface condensation of the compartmental lipids onto the bacterial surface in direct contact and lowers host lipid diffusion by half at the contact area. The direct physical contact under moderate load decreases the area stretch and bending modulus of the host membrane. On the contrary higher bacterial load induces a scaffold-like architecture priming the host compartment for rupture. The degree of bending and area expansion of the phagosome-like compartment is dictated by the ratio of the compartmental surface area available to the surface area of the bacterial contact site. Further direct contact of the bacteria enhances the membranolytic potential of ESAT-6 thus contributing to its virulence. Together we propose that load mediated direct contact of the bacteria drives the switching from spacious to compact phagosome.

149
150 ## RESULTS
151
152 ### Internalization of *Mycobacterium tuberculosis* leads to heterogenous compartmentalization
153 To capture the dynamics of progression of phagosome maturation during mycobacterial infection,
154 we monitored lysosomal marker acquisition in THP1 macrophages infected with live mCherry-
155 expressing *Mycobacterium tuberculosis* (*Mtb*) for different time periods ranging from 2 to 48 hours
156 post-infection (Fig.1a). Over the course of infection, the proportion of compact phago-lysosomes
157 decreased by nearly 50%, while the number of spacious phagosomes stayed relatively constant (Fig.
158 1b). Interestingly, between 2 and 48 hours post-infection, an increase in compact phago-lysosome
159 coincided with a decrease in spacious phago-lysosome, revealing an inverse relationship in their
160 distribution (Fig. 1d, e). This dynamic redistribution suggests that spacious phagosomes may
161 transition into compact phago-lysosome, which then rupture over time, whereas spacious
162 phagosomes remain more stable within the heterogeneous phago-lysosome population.
163 Quantitative image analysis shows a progressive increase in LAMP1 intensity on LAMP1 positive
164 vesicles over time (Supplementary Fig. 1c). This finding is consistent with a previous report
165 highlighting that *Mtb* containing phagolysosome is increasingly marked by LAMP1 with time[35].
166 Morphometric analysis across time points revealed a persistent heterogeneity among LAMP1-
167 positive vacuoles (Supplementary Fig. 1,2,3.), with both compact and spacious phago-lysosome
168 populations present (Fig1. c, Supplementary Fig. 2b, Movie S1, S2). Direct physical contact between
169 *Mtb* and the phago-lysosomal membrane in both compact and spacious states is suggested,
170 regardless of bacterial viability(Fig. 1f-k) The distinct populations of LAMP1-positive vesicles in both
171 dead and live bacterial infections indicates that just the presence of mycobacterial surface in direct
172 physical contact with the phagosomal membrane is sufficient to induce changes in vesicle
173 architecture [35]. This data, thus, suggests that changes in lysosomal marker intensity and vesicular
174 structure are not exclusively dependent on bacterial viability or active secretion of effector proteins.
175 Instead, the physical association between *Mtb* and the host phagosomal membrane might serve as
176 a sufficient trigger for these processes, setting the stage for further pathogen- or host-directed
177 modulation and highlighting the role of the bacterial surface[36].
178
179 ### Direct contact of mycobacteria induces lipid membrane wrapping and creates local diffusion barriers
180 in the host membrane
181 To dissect the role of direct contact of bacteria on host phagosomal membrane shaping and
182 remodelling independent of virulence factor like ESAT-6, we used GFP - *M. smegmatis* as a model
183 organism. We used a method to encapsulate live *Mycobacterium smegmatis* inside giant unilamellar
184 vesicles composed of phagosomal membrane lipids (as described in methods and Supplementary
185 Fig. 4a, b). We optimized electroformation to encapsulate live fluorescent bacteria. This method
186 reduces the impact of external impurities such as oil used in emulsion methods and ensures reliable
187 interaction with host membranes. Despite being avirulent, the fast-growing *M. smegmatis* is
188 considered an ideal surrogate for mycobacterial research[37]. We first quantified the viability of the
189 bacteria in the experimental conditions through colony forming unit (CFU) assay and found it to be

190 ~ 60% (Supplementary Fig. 4c). To capture the dynamics of bacterial interaction in real-time, live
191 bacteria were encapsulated in phagosome membrane mimicking GUVs (40% DOPC, 5.5% DOPE, 22%
192 BSM, 32.5% cholesterol, 0.03% PEG-Biotin) labelled with 0.1% Rhodamine-PE (Rh-PE), immobilized
193 using 0.03% Biotinylated-PEG. Upon monitoring over 60 min, suspended bacteria were found to
194 exhibit random Brownian motion inside the reconstituted phagosome. Interestingly, the area of
195 contact between the bacteria and the host membrane showed an accumulation of host lipids (Fig.
196 5b, Movie S3). Upon visualizing the GUV in 3D at different planes (Fig. 2c and Supplementary Fig.
197 5a, b), we observed lipid wrapping over the bacterial surface area as also illustrated in the schematic
198 diagram (Fig. 2a). Such interaction induces membrane bending at the contact area in both live and
199 dead bacterial surface indicating surface interactions at play. Furthermore, fluorescence recovery
200 of Rh-PE at the bacterial contact site is reduced by ~half following photobleaching in the presence
201 of live bacteria. In contrast, a delayed but full recovery is observed in case of dead bacteria (Fig. 2d),
202 hinting that strong inter-surface interaction between host and live bacteria creates a diffusion
203 barrier. This subsequently leads to lipid segregation within the host membrane. To track the change
204 in lipid reorganization and packaging, we employed two dye model systems (Rh-PE in red and Top-
205 fluor cholesterol in green) and monitored their fluorescence intensity over time (Fig. 2e, Movie S4,
206 Movie S5). We observed that the fluorescence intensity of Top-fluor cholesterol decreases in the
207 vicinity of the contact area (Fig. 2f, h). In contrast, the fluorescence intensity of Rh-PE increases near
208 the contact area, as shown in zoomed images (Fig. 2g, i). Together the live-bacterial direct-contact
209 induces membrane bending, lipid wrapping at the contact area and creates a diffusion barrier
210 resulting in the reorganization of lipids and changes in lipid packing (increased disorderliness) as
211 evident from the marked increase in the fluorescence intensity of Rh-PE in the region [38].
212
213
214 Increasing bacterial load induces membrane disorderliness and global phase separation in the host
215 membrane
216 We next investigated the influence of moderate bacterial load mimicking a spacious phagosome, on
217 the dynamics of the phagosomal membrane. Henceforth, low-to-moderate load and high load
218 mycobacterial conditions are referred to as spacious and compact phagosome mimics, respectively.
219 To capture this, we encapsulated an increased load of bacteria inside the GUV, as illustrated in the
220 schematic (Fig. 3a). We observed that without bacterial load, Rh-PE fluorescence intensity appears
221 to be homogenous throughout the equatorial plane of the membrane. In sharp contrast, in a
222 spacious phagosome mimic, the live bacteria induce striking phase separation in phagosome like
223 compartments as evident from the Rh-PE signal that is restricted to bacterial contact areas (Fig. 3b).
224 However, no significant phase separation was observed in dead bacteria (Supplementary Fig. 6a, b).
225 We observed a change in the fluorescence intensity and thickness of the membrane upon
226 monitoring the GUV mimicking spacious phagosome for 60 minutes (Fig. 3c, Movie S6). Specifically,
227 there is significant mobilization of Rh-PE towards the bottom of the GUV after 60 minutes where
228 the larger pool of bacteria settle down (Fig. 3d, bottom right panel XZ plane). Also, the accumulation
229 of lipids at the bottom of GUVs induces budding at the bottom (Fig. 3d and Supplementary Fig. 7).
230 This suggests that bacteria make the membrane more disordered at the contact areas. Likewise, in

231 both live and dead bacteria condition, the diffusion of Rh-PE on the membrane partially slowed
232 down as evident from the fluorescence recovery after photobleaching at the equatorial plane (Fig.
233 3e). Super-resolution microscopy revealed that the interactions caused by the bacteria hitting and
234 retracting off the host membrane induced higher disorderliness at the point of contact in the GUVs
235 (Fig. 3f) as seen from the Rh-PE signal at the equatorial plane (Fig. 3g). Interestingly, the membrane
236 sustained the disorderliness despite the bacteria having retracted after hitting the surface and were
237 no more in contact. These observations collectively suggest that increasing bacterial load inside the
238 GUV results in stronger interactions with the host membrane via Brownian motion affecting the lipid
239 packing. This subsequently leads to phase separation and the mobilization of Rh-PE at the bottom
240 as more stable contacts get established as the bacteria settles to the bottom due to gravity. This
241 might also impact the mobility of the lipids at other planes as a result of stretching and lipid
242 reorganization in the membrane.
243
244
245 Compact phagosome mimic scaffolds membrane remodelling through bacterial surface-driven
246 condensation
247 The behaviour of Mycobacteria within the confined space of the mycobacteria-containing vacuole,
248 whether in a compact phagosome or during replication, remains poorly understood, particularly
249 with respect to the establishment of direct contact with the host membrane [16]. We hypothesized
250 that a substantial increase in mycobacterial load resembling the formation of bacterial clumps
251 within the phagosome [39] would induce a higher probability of establishing direct-contact with the
252 phagosomal membrane. To examine the impact of clump formation on the phagosome membrane,
253 we encapsulated a significantly higher load of mycobacteria to mimic the compact phagosome,
254 thereby increasing the contact area with the membrane, as illustrated in the schematic (Fig. 4a). To
255 capture the interactions in real-time, we monitored the compact phagosome mimic for 60 minutes.
256 Striking membrane tampering is induced by the random attachment of the bacteria (Fig. 4b, Movie
257 S7). Interestingly, the host membrane remains permanently bent even in the case where the
258 bacteria tend to retract away from their initial contact area. The bacteria exhibit collective mobility
259 as clumps in a compact phagosome mimic compared to that of the spacious phagosome mimic. In
260 line with previous observations, we noted the accumulation of lipids at the bottom of the membrane
261 after 60 minutes (Supplementary Fig. 9 a, b), and subsequent budding at the bottom of the GUV.
262 The budding phenomenon results from phase separation, where the reorganization and
263 mobilization of liquid-disordered lipids induce localized membrane curvature at contact areas
264 making the membrane more deformable (Supplementary Fig. 9 a, b). To establish phase separation,
265 we used two dye systems as previously described, and observed an intense phase separation of the
266 host membrane by the bacteria (Fig. 4c). Next, to visualize the changes in smaller-sized GUVs similar
267 to phagosome size, we encapsulated 4-6 bacteria within smaller GUVs around size 8-10µm.
268 Remarkably, we found that the bacteria caused complete deformation of the membrane
269 (Supplementary Fig. 9c, d). This observation indicates – for a given bacterial load, a higher contact
270 area ina smaller GUV leads to a significantly greater degree of host membrane deformation
271 compared to larger GUVs. This suggests a size-dependent effect, where the smaller volume and

surface area of the GUVs amplify the impact of bacterial interactions, resulting in more pronounced membrane deformations. Super-resolution microscopy reveals the host membrane becomes more disordered at the contact area of the bacteria. The white spots indicate the colocalization point, where the bacteria and host membrane are in contact (Fig. 4d) as evident from the intensity of the overlapping regions of the host and the bacteria (Fig. 4e). Further, the shape of the bacterial clump appears to drive the shape of the host membrane via stretching (Fig. 4f). To investigate the role of bacterial surface on the phase separation of the host lipid membrane, we used a two-dimensional Ising model, where the two states (-1 and +1) represent the lipid ordered and disordered states. Bacterial contacts on the membrane were considered as patches where one kind of lipid has a high probability of accumulating (see Supplementary information for details). We find that when the contacts are few (low bacterial load), global phase separation does not occur. However, the membrane can exhibit local phase separation in the vicinity of the contact site (Fig. 4g). Interestingly, increasing the number of contacts can drive the entire membrane to phase separate (Fig. 4h). The phase separation intensifies as the bacterial contact area on the membrane increases, becoming significantly more pronounced (Fig. 4i). However, increasing the size of bacterial contact on the membrane, keeping the fraction of total area in contact constant, results in a decrease in the degree of phase separation (Fig. 4j-l). This is a consequence of the bacteria-inducing local phase separation. As more bacteria come closer together, there is a significant overlap in the locally phase-separated regions, thereby diminishing the effect on the entire membrane. Bacterial contact-induced phase separation is more pronounced when the lipid interactions are such that the membrane is near the lipid demixing point. (Supplementary Fig. 8a, b, Supplementary text). This suggests that the probability of interaction between bacterial surfaces and the host membrane is influenced by the size of the phagosomal compartment. The disorderliness and degree of phase separation within the membrane are driven by the percentage of bacteria in contact, leading to increased membrane fluidity. As the number of bacteria within a confined volume increase, the probability of interaction and the formation of bacterial clumps also rise. The morphology of the vesicle is determined by the shape of these bacterial clumps (Fig. 3b, f & Supplementary Fig. 9c, d). Further, the fluidized membrane conforms to and wraps around the clumps, resulting in a more rigid scaffold-like structure. Collectively, these concurrent processes are likely to significantly impact membrane parameters.

Mycobacterial load mediated direct contact and ESAT-6 virulence facilitate spacious to compact phagosome switching

We next questioned if there is any correlation between the bacterial load inside the host membrane and the change in the membrane parameters (Fig. 5). To test this, we used micropipette aspiration to aspirate GUVs encapsulating varying loads of the bacteria. The presence of Mycobacteria inside the GUVs was confirmed through bright-field microscopy. Depending on the mobility of the bacteria and shape fluctuation of the GUV, we broadly classified GUVs into Spacious phagosome mimic and Compact phagosome mimic (Fig. 5a-c, Movie S8, Movie S9, Movie S10). Spacious phagosome mimic seems to exhibit higher membrane fluctuations and bacterial motion compared to Compact

313 phagosome mimics and phagosome mimic (i.e., without bacterial load) (Fig. 5a-c, Movie S8, Movie
314 S9, Movie S10). Simultaneously, the geometry (aspiration length L_p and vesical radius R_v, see Fig. 5a,
315 b, c) of the GUV was monitored to document changes in membrane parameters by the interaction
316 of bacteria with the host membrane. Increasing the bacterial load inside the GUV results in a higher
317 probability of establishing bacterial contact with the host membrane as seen in Fig. 3, 4. To quantify
318 these changes in membrane properties, we aspirated Spacious phagosome mimic with a constant
319 change in pressure (i.e., $\Delta P= 50\ Pa$). We observed the aspiration length Lp increases significantly in
320 bacteria loaded spacious phagosome as compared to phagosome mimic without bacteria (Fig. 5a,
321 b, d). Spacious phagosome mimic is found to reduce the area stretch modulus by 5 folds as
322 compared to the phagosome mimic (Fig. 5e). Likewise, the bending modulus of the host membrane
323 is reduced by 6 folds as compared to the phagosome mimic (Fig. 5f). Surprisingly, no change in L_p is
324 observed for the Compact phagosome (Fig. 5c, d). The aspiration length ($L_p = 0$) suggests an absence
325 of direct area expansion, precluding the calculation of both area stretch modulus and bending
326 modulus. Interestingly, significant deposition of host membrane lipid is observed over the surface
327 of the pipette (Fig. 5c, Movie S10). This observation suggests that as the bacterial load increases,
328 the fluidity of the host membrane also increases, leading to greater membrane deformability. In
329 contrast, under high load conditions, bacteria aggregate to form a scaffold-like surface. The fluidized
330 host membrane, influenced by bacterial activity, then wraps around this clump. This interaction
331 collectively results in increased membrane rigidity. These bacterial interactions are efficient in
332 remodelling the membrane properties but are not sufficient for the bacteria to escape from the
333 phagosome membrane.
334 Furthermore, to investigate the role of virulent secretory proteins in bacterial escape, we treated
335 these three conditions with a low concentration (2.5 µM) of monomeric ESAT-6 protein and
336 monitored them for 2 hours. Interestingly, we observed that in this low concentration and the
337 absence of bacteria, there was no significant change in the membrane shape (Fig. 5g, Movie S11).
338 However, spacious phagosome significant budding in the membrane was observed after 60 minutes
339 (0.0667 FPS) (Fig. 5h, Movie S12). As observed in the previous experiment, under a Compact
340 phagosome, the GUV membrane became more rigid compared to the spacious phagosome (Fig. 5c),
341 creating favourable conditions for membrane rupture and bacterial escape from the phagosome.
342 Subsequent treatment with ESAT-6 induces phagosome membrane rupture resulting in bacterial
343 escape (Fig. 5i, Supplementary Fig. 10 a, b, Movie S13). This indicates that bacterial load enhances
344 the membranolytic activity of the virulence factors. The proposed model suggests that direct contact
345 with Mycobacteria affects the maturation of the Mycobacteria-containing vacuole (MCV). This
346 interaction reduces the bending rigidity of the MCV membrane, that might alter the kinetics of
347 maturation machinery, besides enhancing ESAT-6-mediated membrane disruption in a bacterial
348 load-dependent manner.

Discussion

Many intracellular pathogens, including *Mycobacterium tuberculosis* (*Mtb*), manipulate host membranes via secreted effector proteins. However, the role of direct physical contact between bacteria and host membranes and the mechanisms that dictate the pathogen residency time remain unknown[1,40]. Here, we show that bacterial internalization is highly dynamic and heterogeneous, with both compact and spacious LAMP1-positive vacuoles persisting over time, independent of bacterial viability (Fig. 1). Previous studies indicate that internalization is governed not only by host or pathogen specificity but also by the degree of interaction [41]. For *Mtb*, the extent of interaction influences intracellular uptake and contributes to heterogeneous compartmentalization[42-44]. Our findings reveal that *Mtb* exploits direct physical contact with host phagosome membranes to mediate switching from spacious to compact phagosomal state (Fig. 1b,d,e). We demonstrate that this transition is governed by membrane remodelling by bacteria, where bacterial load and contact area serve as determinants of phagosome fate. At low-to-moderate bacterial loads mimicking spacious phagosome-like compartments, a significant reduction in both bending and area stretch moduli is observed accompanied by membrane fluidization and vesiculation. This process initiates when mycobacterial contact induces membrane bending, lipid wrapping and reorganization at the membrane interface, creating diffusion barriers that promote phase [46] (Fig. 2). Notably, these effects are amplified when host membranes are near their lipid lipid demixing point. The change in the Rh-PE and Top-Fluor Cholesterol signal suggests that the bacteria may be extracting cholesterol from the host membrane as *Mycobacteria* are known to scavenge cholesterol from the host for their metabolism [45]. Indeed intracellular vacuolar compartments represent soft confinements that can be subjected to remodelling and deformation by localized forces such as the active propulsion by motile bacteria[46].

The extent of host membrane phase separation depends on bacterial load (Fig. 2-4). Under spacious phagosome mimics, freely moving bacteria contacting the membrane at multiple planes induced fluidization and disordered protrusions (Fig. 3d,e). In contrast, compact phagosome mimics with higher bacterial load cause global reshaping and complete phase separation driven by bacterial clumping (Fig. 4b). The phagosome membrane's proximity to a lipid demixing point further enhances phase separation upon bacterial contact (Fig. 3b). Indeed, previous studies [47-51] have suggested that cell membranes lie close to the lipid demixing point[52]. Bacterial surface may induce condensation of host membrane interfaces that are close to the lipid demixing point driving phase separation. Such a phenomena might also explain the lipid zippering proposed for bacterial surface lectin LecA with the host cell glycosphingolipid Gb3 sufficient for driving complete internalization of the *Pseudomonas aeruginosa* [5]. Self-propelling motile bacteria are known to induce stronger non-equilibrium fluctuations in the membrane, resulting in the formation of long protruding tubes [30]. Unlike motile bacteria, host membrane deformation by mycobacteria is driven by inter-surface interactions and dictated by the ratio of available surface area of the host membrane and the area of direct-contact. Importantly, this mechanical priming synergizes with ESAT-6 activity, as the softened membrane becomes more susceptible to the effects of the virulence factor. Load dependent shape deformations of encapsulated giant vesicles have also been observed for self-

propelled janus colloids that induce highly branched tether-like protrusions at low/moderate loads and globular reshaping at higher loads capturing vesicle shapes that do not exist in equilibrium systems [53].

The striking change in the area stretch modulus and the bending modulus of the compartmental membrane with respect to the bacterial load not only renders it more deformable but also might influence the dynamics of phagosome maturation. Under spacious phagosome mimic, ESAT-6 activity induces membrane vesiculation, reducing the available area of the host membrane (Fig. 4h), that may eventually progress into a compact phagosome mimic (Fig. 5i). This ultimately leads to phagosome rupture, similar to the effects observed under high bacterial load conditions (Fig. 5i). Vesiculation may represent a transient intermediate in the conversion from spacious to compact phagosomes. Such compact phagosome compartments preferentially facilitate the activity of secreted virulence factors, thereby promoting *Mtb* access to the host cytosol [44]. ESAT-6 has been reported to induce independent events like vesiculation and leakage [54]. The ESX-1 secretion system facilitates direct interaction with host membranes[23], and targeting sterol-rich microdomains to disrupt the Mycobacterium-Containing Vacuole (MCV)[55]. The bending modulus and tension of the membrane are known to regulate the binding kinetics of proteins, the shape generation of the membrane during endocytosis as well as the rate of budding for inter-organelle trafficking [56-58]. The direct-contact mediated manipulation of the phagosomal compartment could facilitate ESAT-6-mediated disruption while potentially delaying phagosome maturation. Indeed, the binding of Ras family proteins is known to be sensitive to membrane tension [56, 59]. The mechanical properties of the membranes are critical for processes involving fission and fusion of membranes [57, 60, 61]. Together, we propose that the ability to switch from spacious to compact states may represent an evolved strategy allowing *Mtb* to either persist within protective compartments or escape into the cytosol when conditions favor rupture regulating their intracellular residency time.

Material & Methods

Materials

1,2-Dioleoyl-sn-glycero-3-phosphocholine (DOPC), 1,2-dioleoyl-sn-glycero-3-phosphoethanolamine (DOPE), BSM, di-stearoyl phosphatidyl ethanolamine-PEG (2000)-biotin, and cholesterol were obtained from Avanti Polar Lipids. The fluorescent lipid lissamine rhodamine B sulfonyl (Liss Rhod PE) and Top-fluor cholesterol were also sourced from Avanti Polar Lipids. Avidin-coated chamber slides were acquired from Sigma-Aldrich.

Preparation of GUV

Giant unilamellar vesicles (GUVs) that imitate the phagosomal membrane were made up of 40% DOPC, 5.5% DOPE, 22% BSM, 32.5% cholesterol, 0.03% PEG-Biotin, and 0.1% Rhod PE. GUVs were created by getting and slightly altering the protocol given in[57]. In summary, conductive ITO-coated glass from Nanion Technologies, GmbH was equally covered with 15µL of the lipid mixture at a concentration of 5 mg/ml, and it was vacuum-dried for a minimum of three hours. After rehydrating the dried lipid film in 300 ± 5 mOsm sucrose solution of pH (6-6.5), the GUVs developed for three hours at 40-45°C with a sine voltage of 2V and 10 Hz. Using 7H9 media containing precultured Mycobacteria, the lipid film was rehydrated in order to encapsulate live Mycobacteria within the GUVs.

For encapsulation experiments, *Mycobacterium* cultures were grown in 7H9 medium to an optical density OD of 1.0–1.2. The bacterial suspension was subsequently used for encapsulation within giant unilamellar vesicles (GUVs). To assess bacterial viability under the experimental conditions, colony-forming unit (CFU) assays were performed, which indicated that approximately 60% of the encapsulated bacteria remained viable.

Microscopy

An 8-well Ibidi chamber slide was coated with 10µl of 1 mg/ml streptavidin, followed by the addition of 200µL of biotinylated GUVs. The GUVs were then incubated for 15 minutes to cause immobilisation. Leica TCS SP8 LCSM imaging was carried out with the proper Rhodamine-PE (561 nm) and Alexa-488 (488 nm) laser. Every experiment was conducted using the same laser power and gain settings.

Initially, images were taken with a lower laser intensity for the Fluorescence Recovery after Photobleaching (FRAP) measurements. A 5µm radius of bleaching was achieved within the chosen ROI after 30 seconds of photobleaching at maximum laser power. The recovery curve was then measured, and the laser intensity was adjusted to the attenuated level. The GUV under visualisation was photobleached at its equatorial plane. Following three repetitions, the FRAP curves were standardised for each condition.

Expression and Purification of ESAT-6

The ESAT-6 protein was expressed using the Escherichia coli BL21 (DE3, pLysS) strain. The strain was transformed with the plasmid pET22b containing the *Mycobacterium tuberculosis* gene Rv3875, which encodes the ESAT-6 protein. Transformed cells were grown in Luria-Bertani (LB) medium at 37°C until the optical density at 600 nm (OD600) reached approximately 0.6. Protein expression was induced by adding 1 mM isopropyl β-D-1-thiogalactopyranoside (IPTG), followed by overnight incubation at 18°C. Post-induction, the bacterial cells were harvested by centrifugation and lysed via sonication. The cell lysate was then subjected to affinity purification using nickel-nitrilotriacetic

acid (Ni-NTA) resin, per the manufacturer's instructions (GE Healthcare, UK). The eluted fractions containing the His-6-tagged ESAT-6 protein were analysed using SDS-PAGE to confirm protein purity. Purified fractions were subsequently dialyzed against an appropriate buffer, concentrated, and stored at -80°C in aliquots for further use.

Micropipette Aspiration

Using a 100X objective lens, all measurements were made using an Olympus IX83 epifluorescence microscope fitted with Hoffman modulation optics. Three-axis hydraulic micromanipulators are utilised to position the pipette. Capillaries with a diameter of 10µm are used to extract micro-pipettes (Narashige Micro Forge MF-900, Sutter Instruments CO P-87). On top of the unfinished DIY coverslip, 100 µl of GUVs were put. The suction pressure P applied to a bilayer vesicle produces a uniform membrane tension (τ), which is described by a geometric relation based on the pipet (Radius)$R_{pipette}$ and vesicle (Radius)R_{GUV} of the vesicle spherical segment exterior to the pipette,

$$\tau = (1/2)*(R_{pipette}\Delta P)/(1-(R_{pipette}/R_{GUV}))$$

[62, 63]. Movement of the projection length L_p inside the pipette directly measures the area increase. Using measurements of the vesicle spherical segment and cylindrical projection dimensions, we numerically computed changes in apparent area Δa for each displacement ΔL_p of the projection length with simple geometric formulae and the constraint of a fixed vesicle volume [64]. The proportionality between apparent area and length is easily seen in the following first-order approximation:

$$\Delta a = 2\pi * R_{pipette} * \Delta L_p + 2\pi R_{pipette}^2$$

While the reference area $a_0 = 4\pi * R_{GUV}^2$ corresponds to a spherical vesical radius $R_{GUV.}$ These formulas combine to give the following expression for the areal strain:

$$\Delta a/a_0 = (R_{pipette}^2 * (1+L_p/ R_{pipette}))/2R_{GUV}^2$$

Displacement of the projection length of an aspirated vesicle under a change in suction pressure is shown in Fig.4d. Even though the apparent area can be measured over a tension range from 76 µN/m to 550 µN/m as demonstrated in Fig. 4e to determine the area stretch modulus (K_a), we plot the change in tension (τ) against direct area of expansion, and the resulting slope is $K_{a.}$to determine the bending modulus (K_b), we plot the semi-log of tension(τ) against the direct area of expansion, and resulting slope is $K_{b.}$ All the experiments were performed at room temperature[64].

Image Analysis

Image analysis and processing were done using the ImageJ program. The average fluorescence intensity was quantified using the line intensity profiling at the direct contact sites along the equatorial plane of GUVs. The same detection configuration was followed for every experiment. Every experiment set used the same detection configuration. ImageJ was used to manually quantify the diameters of the vesicles.

Mycobacterial strains and growth conditions

M. tuberculosis H37Rv expressing mCherry strains were grown in Middlebrook 7H9 (BD Difco 271310) supplemented with 10% OADC (BD Difco 211886) at 37 °C. Before infection, bacterial

509 clumps were removed by centrifugation at 80 × g and supernatant was pelleted, re-suspended in
510 RPMI media, and used for infection, as discussed previously [65]. All the experiments were performed
511 inside a BSL-3 facility.
512
513
514 **Cell culture and infection**
515 THP-1 monocytes were cultured in RPMI 1640 (Gibco™ 31800022) supplemented with 10% fetal
516 bovine serum (Gibco™ 16000-044). THP1 monocytes were differentiated to macrophages by
517 treatment with 20 ng/ml of phorbol myristate acetate (PMA) (Sigma-Aldrich, P8139) for 24 h
518 followed by incubation in PMA-free RPMI 1640 medium for 24 hours and used for infections. THP-1
519 monocyte-derived macrophages were incubated with mycobacteria at an MOI of 10 for 2 h followed
520 by the removal of extracellular bacteria by multiples washes. Infected cells were fixed with 4%
521 paraformaldehyde (Sigma 158127) at 2, 6, 12, 24 and 48 hpi and were used for subsequent
522 experiments.
523
524 **Immunostaining, imaging, and image analysis**
525 For immunostaining of LAMP1 marker, differentiated THP-1 macrophages after infection were fixed
526 with 4% paraformaldehyde, washed with PBS, and permeabilized with SAP buffer (0.2% saponin
527 (Sigma-Aldrich S4521), 0.2% gelatin (Himedia Laboratories TC041) in PBS) for 10 min at room
528 temperature. Primary antibody Lamp1 (DSHB, clone H4A3) was prepared in SG-PBS (0.02% saponin,
529 0.2% gelatin in PBS) and incubated at room temperature for 2 hours. After washing with SG-PBS,
530 cells were incubated in AlexaFluor 647 (Life Technologies, Invitrogen) prepared in SG-PBS for 1 h at
531 room temperature, washed, stained with 1 µg/ml of 4[prime],6-diamidino-2-phenylindole (DAPI) for
532 30 minutes at room temperature. The coverslips were then mounted using a Mowiol-based
533 mountant and imaged using Olympus FV3000 confocal microscope using a 60x objective.
534 Images were analyzed by CellProfiler 4.2.8. and pipelines similar to those previously established[66]
535 were used. In all cases, images were segmented to identify nuclei, cells, bacteria, and Lamp1-
536 positive compartments. Objects such as bacteria and Lamp1-positive vesicles were related to
537 individual cells to obtain single cell statistics, and multiple parameters relating to their numbers,
538 sizes, intensities, as well as *Mtb*-Lamp1 associations were extracted. MS Excel and GraphPad 8.0.1
539 were used for data analysis and plotting graphs. Statistical significance between different sets was
540 determined using Mann-Whitney unpaired test *t* test with unequal variance.
541

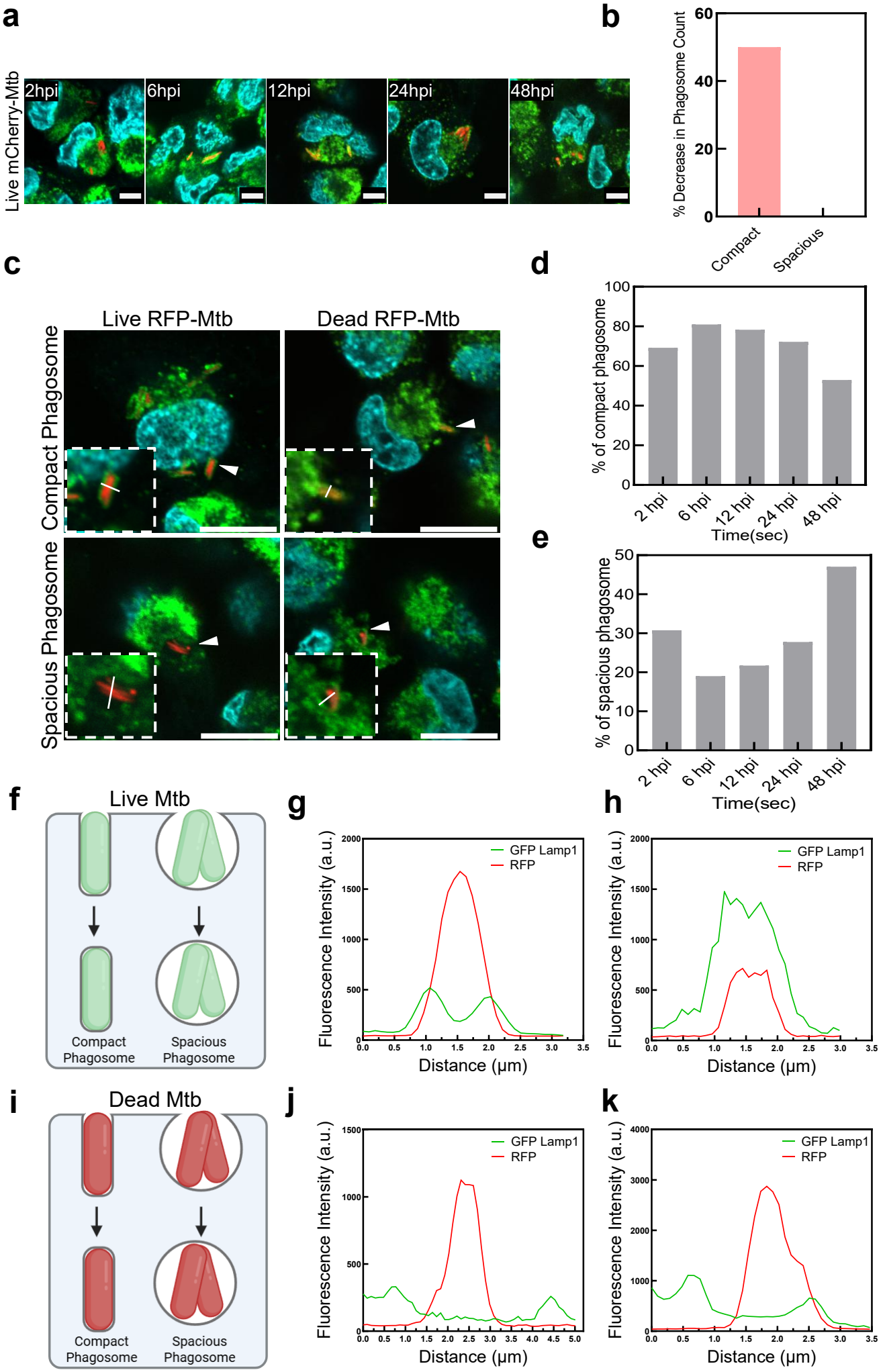
a
Live mCherry-Mtb
2hpi
6hpi
12hpi
24hpi
48hpi
b
% Decrease in Phagosome Count
60
40
20
0
Compact
Spacious
c
Live RFP-Mtb
Dead RFP-Mtb
Compact Phagosome
Spacious Phagosome
d
% of compact phagosome
100
80
60
40
20
0
2 hpi
6 hpi
12 hpi
24 hpi
48 hpi
Time(sec)
e
% of spacious phagosome
50
40
30
20
10
0
2 hpi
6 hpi
12 hpi
24 hpi
48 hpi
Time(sec)
f
Live Mtb
Compact Phagosome
Spacious Phagosome
g
Fluorescence Intensity (a.u.)
GFP Lamp1
RFP
Distance (μm)
h
Fluorescence Intensity (a.u.)
GFP Lamp1
RFP
Distance (μm)
i
Dead Mtb
Compact Phagosome
Spacious Phagosome
j
Fluorescence Intensity (a.u.)
GFP Lamp1
RFP
Distance (μm)
k
Fluorescence Intensity (a.u.)
GFP Lamp1
RFP
Distance (μm)

Figure Legends

Figure 1.

Lamp1 co-localization with *Mtb* increases with time and forms heterogenous populations of compact and spacious phagosomes

a. Confocal imaging of THP-1 cells infected with Live *Mtb* tagged with *Mtb* tagged with mCherry (red) and immunostained for Lamp1 (green) and fixed with 4% paraformaldehyde/PBS at timepoints- 2, 6, 12, 24 and 48hrs post-infection (hpi). Scale bar, 10µm. Representative images of two technical replicates from one independent experiment. (no. of Lamp1 associated *Mtb* = 100). **b.** Comparison of percentage changes in phagosome counts obtained from manual segmentation shows a progressive decline in compact phagosomes up to 48 hpi, while spacious phagosomes remain relatively unchanged. **c.** Representative images for compact and spacious morphology of Lamp1 vesicles encapsulating *Mtb* in infected cells. Scale bar, 10µm. ROI drawn across the structure in ImageJ to retrieve the intensity plot. **d.** Comparison of percentage of compact phagosomes with live *Mtb* obtained from manual segmentation in infected cells till 48hpi. **e.** Comparison percentage of spacious phagosomes and live *Mtb* obtained from manual segmentation in exist in infected cells till 48hpi. **f.** Schematic representation of compact and spacious phagosome in vesicles encapsulating Live *Mtb* in infected cells. **g,h.** Intensity plots of *Mtb* (red) and Lamp1 (green) shows the distribution of fluorescence in compact phagosomes where Lamp1 closely colocalizes with *Mtb* shown by the overlapping of signal peaks. (no. of compact phagosomes = more than 100) **i.** Schematic representation of compact and spacious phagosome in vesicles encapsulating dead *Mtb* in infected cells. **j, k.** Intensity plots of *Mtb* (red) and Lamp1 (green) shows the distribution of fluorescence in spacious phagosomes where Lamp1 and *Mtb* signal peaks show no overlapping. (no. of compact phagosomes = 50)

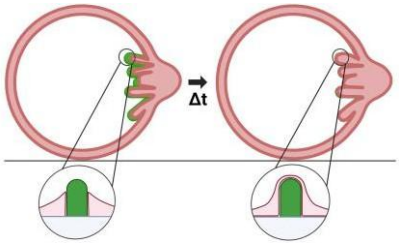
a
Δt

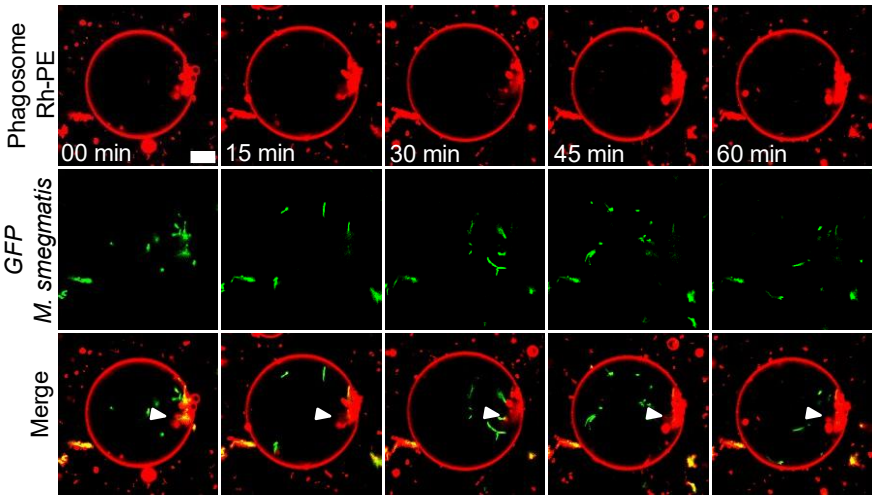
b
Phagosome Rh-PE
GFP M. smegmatis
Merge
00 min
15 min
30 min
45 min
60 min

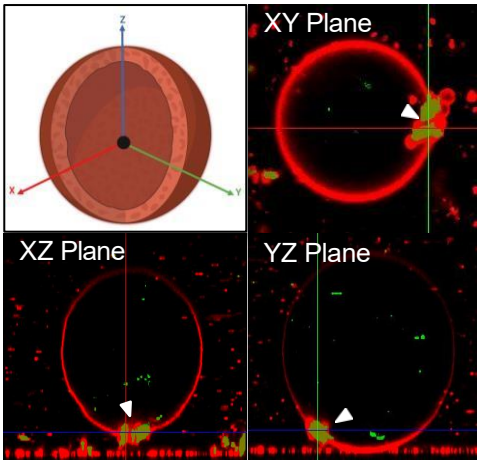
c
XY Plane
XZ Plane
YZ Plane

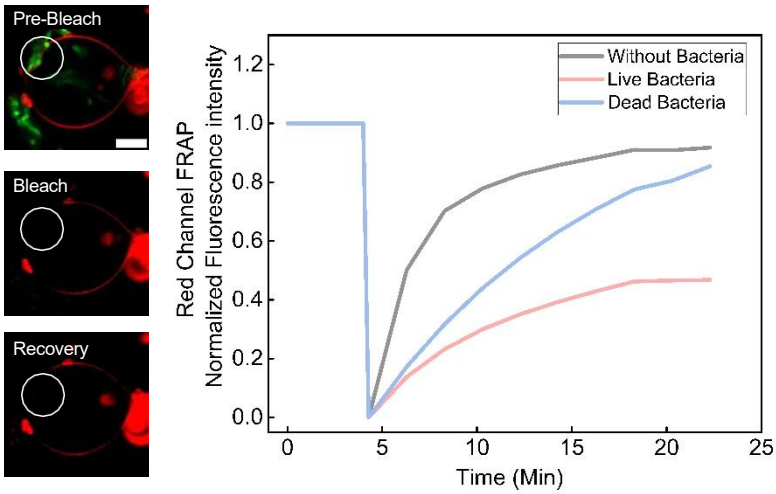
d
Pre-Bleach
Bleach
Recovery
Red Channel FRAP
Normalized Fluorescence intensity
Without Bacteria
Live Bacteria
Dead Bacteria
Time (Min)

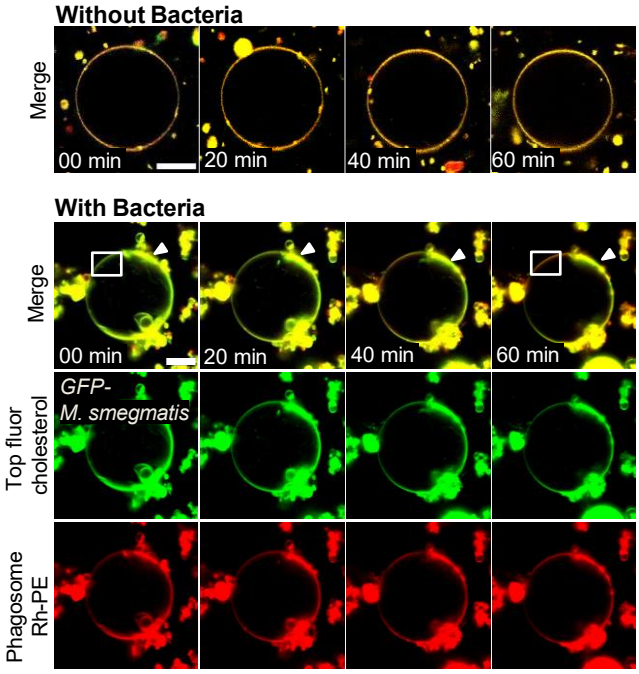
e
Without Bacteria
Merge
00 min
20 min
40 min
60 min
With Bacteria
Merge
GFP-M. smegmatis
Top fluor cholesterol
Phagosome Rh-PE

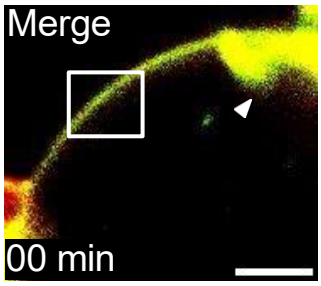
f
Merge
00 min

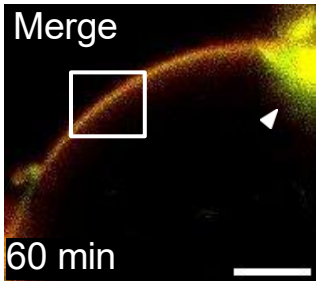
g
Merge
60 min

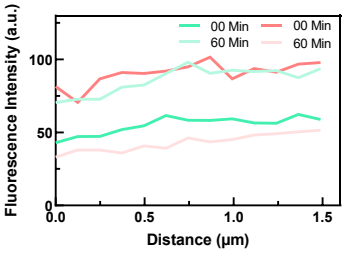
h
Fluorescence Intensity (a.u.)
00 Min
60 Min
00 Min
60 Min
Distance (μm)

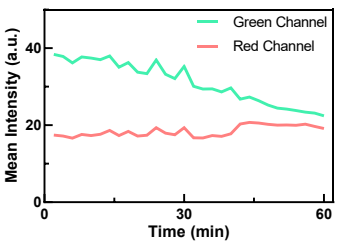
i
Mean Intensity (a.u.)
Green Channel
Red Channel
Time (min)

Figure 2.

Direct surface contact of *Mycobacterium smegmatis* triggers lipid wrapping and creates diffusion barrier in the phagosome membrane

a. Schematic representation of the experimental design depicting the impact of direct contact on immobilized GUV mimicking host phagosomal membrane. **b.** Time-lapse confocal imaging of GUVs labelled with 0.1% Rh-PE (red) and immobilized using 0.03% PEG-Biotin encapsulated with live *M. smegmatis-GFP* (green). Scale bar, 10µm. Representative images from three independent experiments. (no. of GUVs = 30-35). **c.** Schematic representation and XYZ Projection of the mycobacteria-mediated curvature change from b. **d.** Mean fluorescence recovery curve after photobleaching experiments of direct contact of bacteria (live and dead) on the membrane. Data points using mean values from three independent experiments. Scale bar, 5µm **e.** Time-lapse confocal imaging of GUVs of phagosomal membrane composition labelled with 0.05% Rh-PE (red) and 0.05% Top Fluor cholesterol (green) and immobilized using 0.03% PEG-Biotin encapsulated with live *M. Smegmatis* (green). Scale bar, 10µm. Images are the representation from three independent experiments. (no. of GUVs = 30-35). Zoomed image of confocal images of region near to direct contact of bacteria at **f.** 0 mins, **g.** 60 mins (Scale bar: 5µm.). White box in e indicates the region for line intensity profile at respective time points. **h.** Fluorescence intensity profile of Topfluor cholesterol (green shades) and Phagosome Rh-PE (Red shades) at two different time points. **i.** Mean fluorescence intensity profile of green channel (Topfluor cholesterol) and red channel (Phagosome Rh-PE).

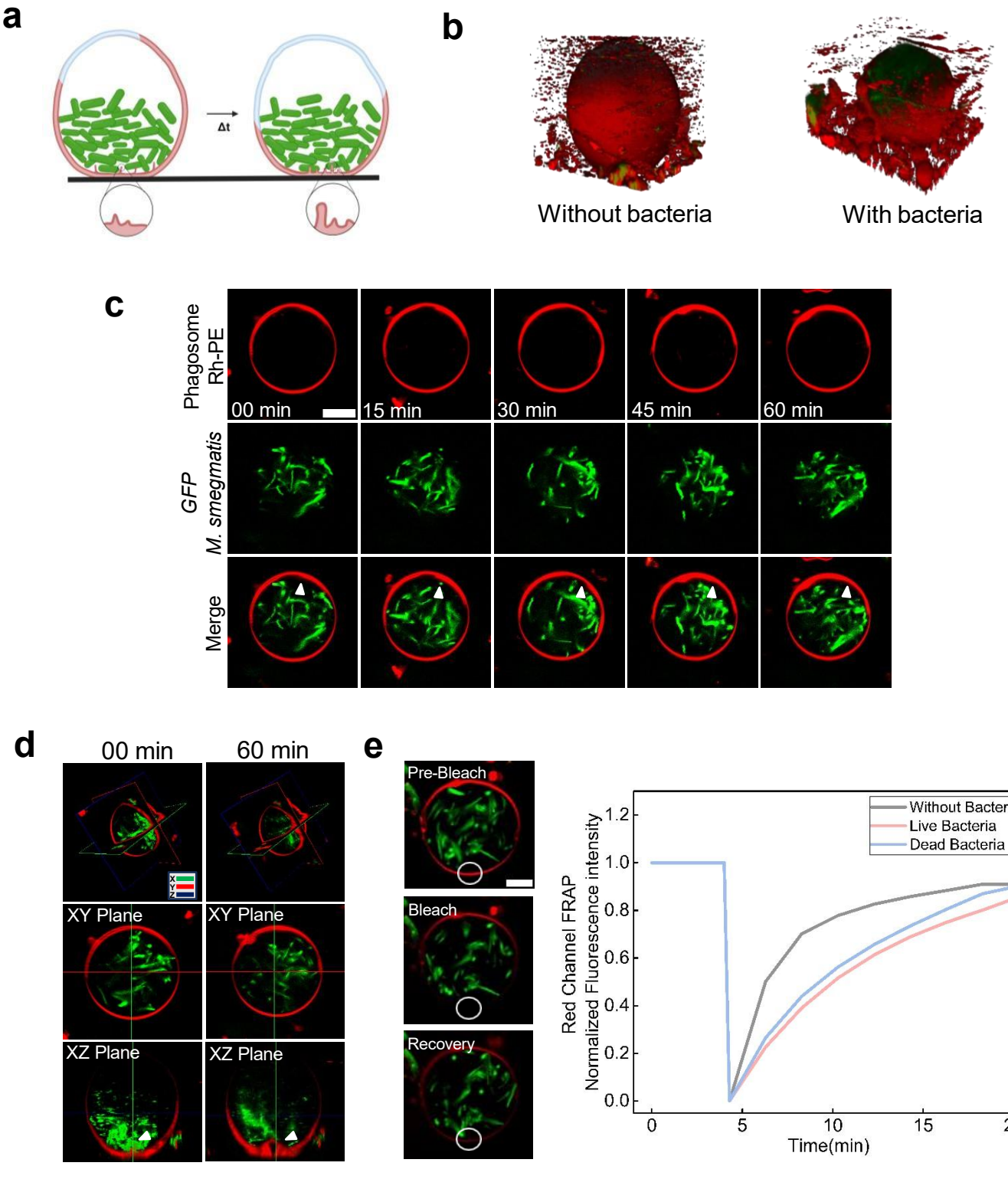
a
Δt
b
Without bacteria
With bacteria
c
Phagosome Rh-PE
GFP M. smegmatis
Merge
00 min
15 min
30 min
45 min
60 min
d
00 min
60 min
XY Plane
XY Plane
XZ Plane
XZ Plane
e
Pre-Bleach
Bleach
Recovery
Red Channel FRAP Normalized Fluorescence intensity
Time(min)
Without Bacteria
Live Bacteria
Dead Bacteria
f
1
2
g
Fluorescence Intensity (a.u.)
Distance (μm)
Rh-PE
GFP
1
2

Figure 3.

Increasing mycobacterial load induces global phase separation in the phagosome membrane

a. Schematic representation for the experimental design depicting the impact of a spacious phagosome mimic on immobilized GUV mimicking host phagosomal membrane. **b.** 3D projection of vesicle without and with bacteria exhibiting the bacteria-induced phase separation (no. of GUVs = 30-35). **c.** Time- lapse confocal imaging of GUVs labelled with 0.1% Rh-PE (red) and immobilized using 0.03% PEG-Biotin Biotin mimicking spacious phagosome encapsulated with live *M. smegmatis* (green). Scale bar, 10µm. Representative images from three independent experiments. (no. of GUVs = 30-35). **d.** XYZ Projection of the mycobacteria load mediated changes from c representing the budding event over time. **e.** Mean fluorescence recovery curve after photobleaching experiments of spacious phagosome mimic GUVs on the membrane. Data points using mean values from three independent experiments. Scale bar, 5µm **f.** Structured illumination microscopy (SIM) images of GUVs labelled with 0.1% Rh-PE (red) and immobilized using 0.03% PEG-Biotin encapsulated with moderate load of live *M. smegmatis* (green), 5µm. (no. of GUVs = 30-35). Line intensity plots in **g**. of line 1 and 2 respectively.

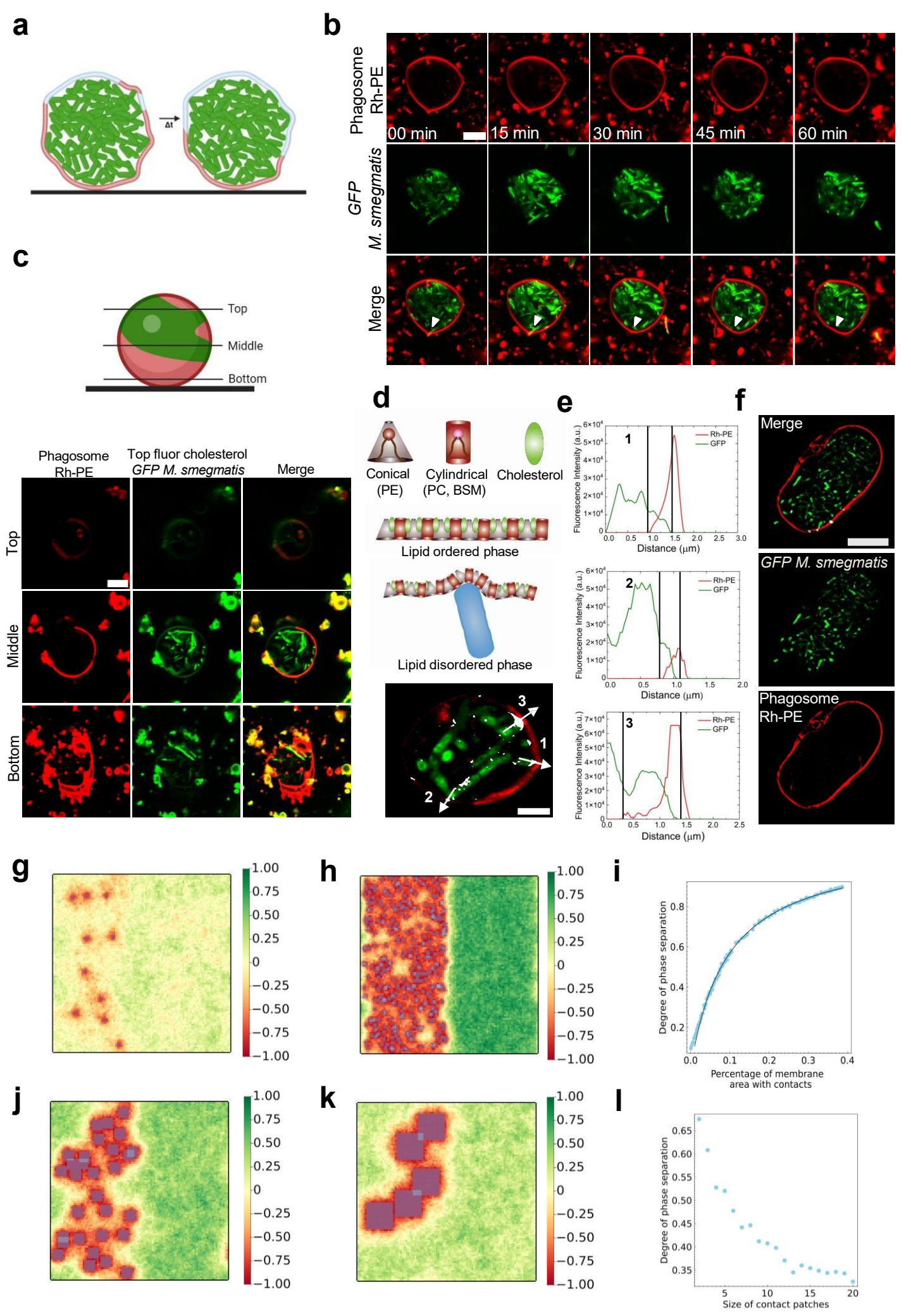
a
Δt
b
Phagosome Rh-PE
GFP M. smegmatis
Merge
00 min
15 min
30 min
45 min
60 min
c
Top
Middle
Bottom
Phagosome Rh-PE
Top fluor cholesterol GFP M. smegmatis
Merge
Top
Middle
Bottom
d
Conical (PE)
Cylindrical (PC, BSM)
Cholesterol
Lipid ordered phase
Lipid disordered phase
1
2
3
e
Rh-PE
GFP
Fluorescence Intensity (a.u.)
Distance (μm)
f
Merge
GFP M. smegmatis
Phagosome Rh-PE
g
h
i
Degree of phase separation
Percentage of membrane area with contacts
j
k
l
Size of contact patches

Figure 4.

Compact phagosome mimic induces host membrane remodelling through condensation driven by bacterial surface interactions

a. Schematic representation of the experimental design depicting the impact of a compact phagosome mimic on immobilized GUV mimicking phagosomal membrane. **b.** Time-lapse confocal imaging of GUVs labelled with 0.1% Rh-PE (red) and immobilized using 0.03% PEG-Biotin mimicking Compact phagosome encapsulated with live *M. smegmatis* (green). Scale bar, 10µm. Representative images from three independent experiments (no. of GUVs = 30-35). **c.** Schematic representation and XY plane of the GUV of phagosomal membrane composition labelled with 0.05% Rh-PE (red) and 0.05% Top-Fluor cholesterol (green) and immobilized using 0.03% PEG-Biotin Biotin mimicking Compact phagosome encapsulated with live *M. Smegmatis* (green) representing different planes. Scale bar, 10µm. Images are the representative of three independent experiments. (no. of GUVs = 30-35). **d**. Structured illumination microscopy (SIM) images of GUV, white spot showing degree of colocalization. **e.** Showing line intensity graph plot for Rh-PE (red channel) and GFP (green channel) and marked area with black line denote overlapping region of red and green channel. For the colocalization the points are mentioned in d. **f.** Structured illumination microscopy (SIM) images of GUVs with high bacterial load showing distortion of shape (no. of GUVs = 30-35). Time-averaged state of the membrane. **g.** With a low load, phase separation is observed only near the contacts. Degree of phase separation 0.137 (N_c = 10, p=2). **h.** With a high load, global phase separation is seen. Degree of phase separation 0.675 (N_c=300, p=2). **i.** Degree of phase separation in the membrane as a function of the percentage of membrane area in contact with the membrane. **j,k,l.** Varying the contact patch size, keeping the fraction of membrane area in contact fixed. j & k show representative time-averaged states for p=6 and p=15 respectively. (Parameters in all figures: N=100, φ=0.5, J/k_BT=0.4, h/k_BT=5.0)

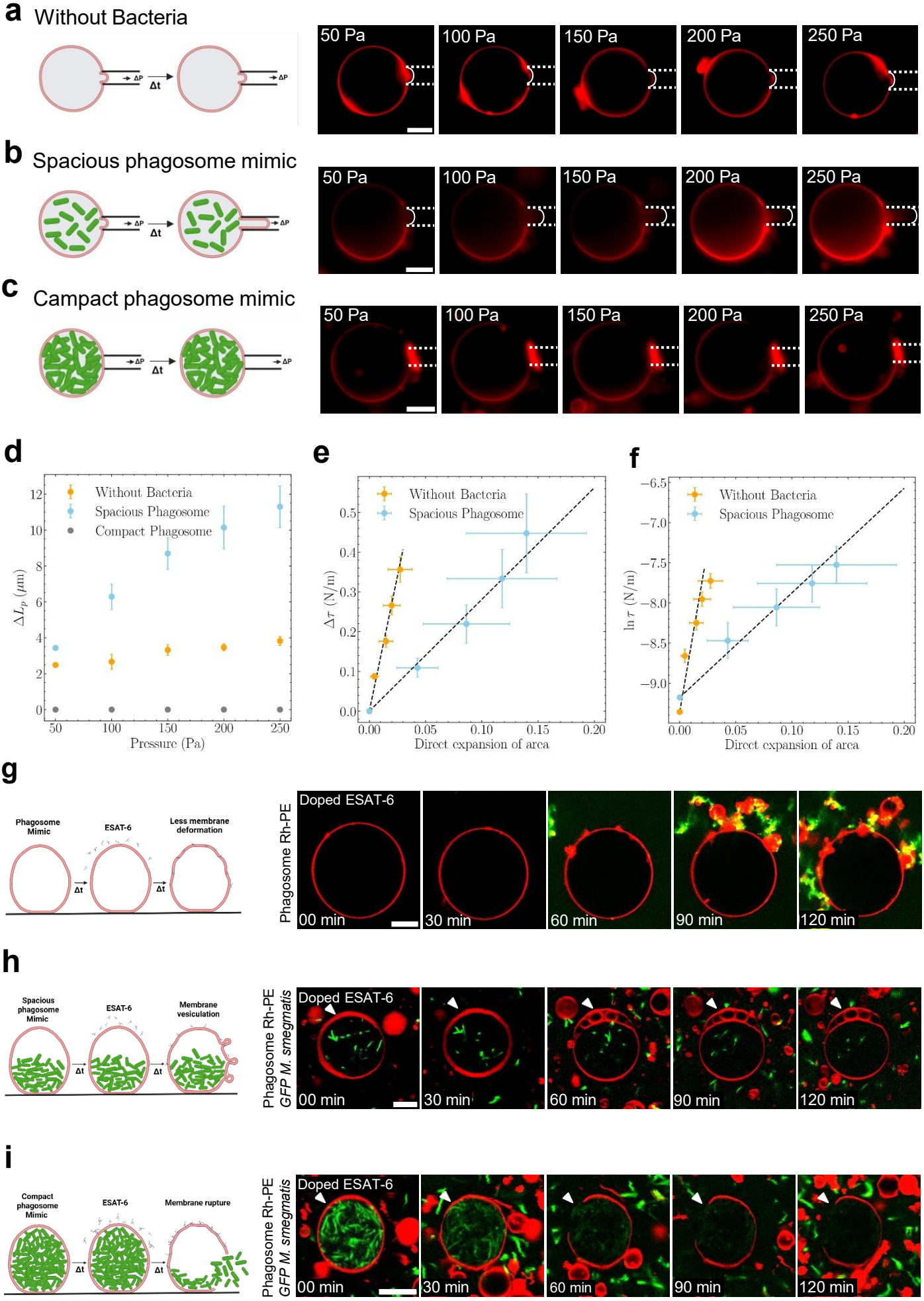
a
Without Bacteria
ΔP
Δt
ΔP
50 Pa
100 Pa
150 Pa
200 Pa
250 Pa
b
Spacious phagosome mimic
ΔP
Δt
ΔP
50 Pa
100 Pa
150 Pa
200 Pa
250 Pa
c
Campact phagosome mimic
ΔP
Δt
ΔP
50 Pa
100 Pa
150 Pa
200 Pa
250 Pa
d
Without Bacteria
Spacious Phagosome
Compact Phagosome
ΔL_p (μm)
Pressure (Pa)
e
Without Bacteria
Spacious Phagosome
$\Delta\tau$ (N/m)
Direct expansion of area
f
Without Bacteria
Spacious Phagosome
$\ln\tau$ (N/m)
Direct expansion of area
g
Phagosome Mimic
ESAT-6
Less membrane deformation
Δt
Δt
Phagosome Rh-PE
Doped ESAT-6
00 min
30 min
60 min
90 min
120 min
h
Spacious phagosome Mimic
ESAT-6
Membrane vesiculation
Δt
Δt
Phagosome Rh-PE
GFP M. smegmatis
Doped ESAT-6
00 min
30 min
60 min
90 min
120 min
i
Compact phagosome Mimic
ESAT-6
Membrane rupture
Δt
Δt
Phagosome Rh-PE
GFP M. smegmatis
Doped ESAT-6
00 min
30 min
60 min
90 min
120 min

716 **Figure 5.**
717 Direct surface contact of mycobacteria enhances the virulence of ESAT-6 and facilitates spacious
718 to compact phagosome switching
719
720 **a.** Schematic representation and time-lapse Epi-fluorescence imaging of GUVs labelled with 0.1%
721 Rh-PE (red). Scale bar, 10µm. Aspirated with Pressure (Δp = 50Pa) and monitored over time.
722 Representative images from three independent experiments. **b.** Schematic representation and
723 time-lapse Epi-fluorescence imaging of GUVs labelled with 0.1% Rh-PE (red) mimicking spacious
724 phagosome with live *M. smegmatis* (green). Scale bar, 10µm. Aspirated with Pressure (Δp = 50Pa)
725 and monitored over time. Representative images from three independent experiments. **c.**
726 Schematic representation and Time-lapse Epi-fluorescence imaging of GUVs labelled with 0.1% Rh-
727 PE (red) mimicking compact phagosome with live *M. smegmatis* (green). (green). Scale bar, 10µm.
728 Aspirated with Pressure (Δp = 50Pa) and monitored over time. Representative images from
729 biologically three independent experiments. **d.** Plot for the length of protrusion(ΔL_P) vs pressure (P)
730 from a,b and c. Data points shown are the Means ± SD of three independent experiment. **e.**
731 Quantifying the area stretch modulus(k_a) from the change in tension(Δτ) vs direct expansion of area
732 plot from a, b and c. Orange and blue spots with bars: experimental points for without bacteria and
733 Spacious phagosome, respectively, average ± SD. Dotted line: Linear fit, y= a*x+b, for without
734 bacteria a = 13.5 ± 1.09, b = (-1.25 ± -0.49)*10^{-6} , R^2 = 0.125 and for Spacious phagosome a = 2.81 ±
735 0.10 b.(-1.81 ± 0.727)*10^{-7}, R^2 = 0.056455, $K_{a(without\ bacteria)}$ = 13.5 ± 1.09mN/m $K_{a(Spacious\ phagosome\ )}$ =
736 2.81 ± 0.10 mN/m **f.** Quantification of the bending modulus (k_b) from the semi-log plot of tension
737 versus direct expansion of area from a, b, c. Orange and blue spots with bars: experimental points
738 for without bacteria and Spacious phagosome, respectively, average ± SD. Dotted line: Linear fit y=
739 a*x+b, for without bacteria a = 81.52 ± 1.489 , b = -2.45 ± (6.74*10^{-6}), R^2 = 0.605 and for Spacious
740 phagosome a = 13.021 ± 0.9696, b = -2.27 ± (4.28*10^{-7}), R^2 =- 0.097, $K_{b(without\ bacteria)}$ =(1.33 ±
741 0.022)*10^{-20} J, $K_{b(Spacious\ phagosome)}$ = (0.21±0.02)*10^{-20} J **g.** Time-lapse confocal imaging of GUVs
742 labelled with 0.1% Rh-PE (red) and immobilized using 0.03% PEG-Biotin incubated with 2.5µM
743 doped FITC-ESAT-6 (green). Scale bar, 10µm.Images are representative of 3 independent
744 experiments (no. of GUVs = 30-35). **h.** Time-lapse confocal imaging of GUVs labelled with 0.1% Rh-
745 PE (red) and immobilized using 0.03% PEG-Biotin encapsulated with moderate load of live *M.*
746 *smegmatis* (green) and incubated with 2.5µM doped FITC-ESAT-6 (green). Scale bar, 10µm.Images
747 are representative of 3 independent experiments (no. of GUVs = 30-35). **i.** Time-lapse confocal
748 imaging of GUVs labelled with 0.1% Rh-PE (red) and immobilized using 0.03% PEG-Biotin
749 encapsulated with high load of live *M. smegmatis* (green) and incubated with 2.5µM doped FITC-
750 ESAT-6 (green). Scale bar, 10µm (no. of GUVs = 10-15).
751
752
753
754
755
756
757

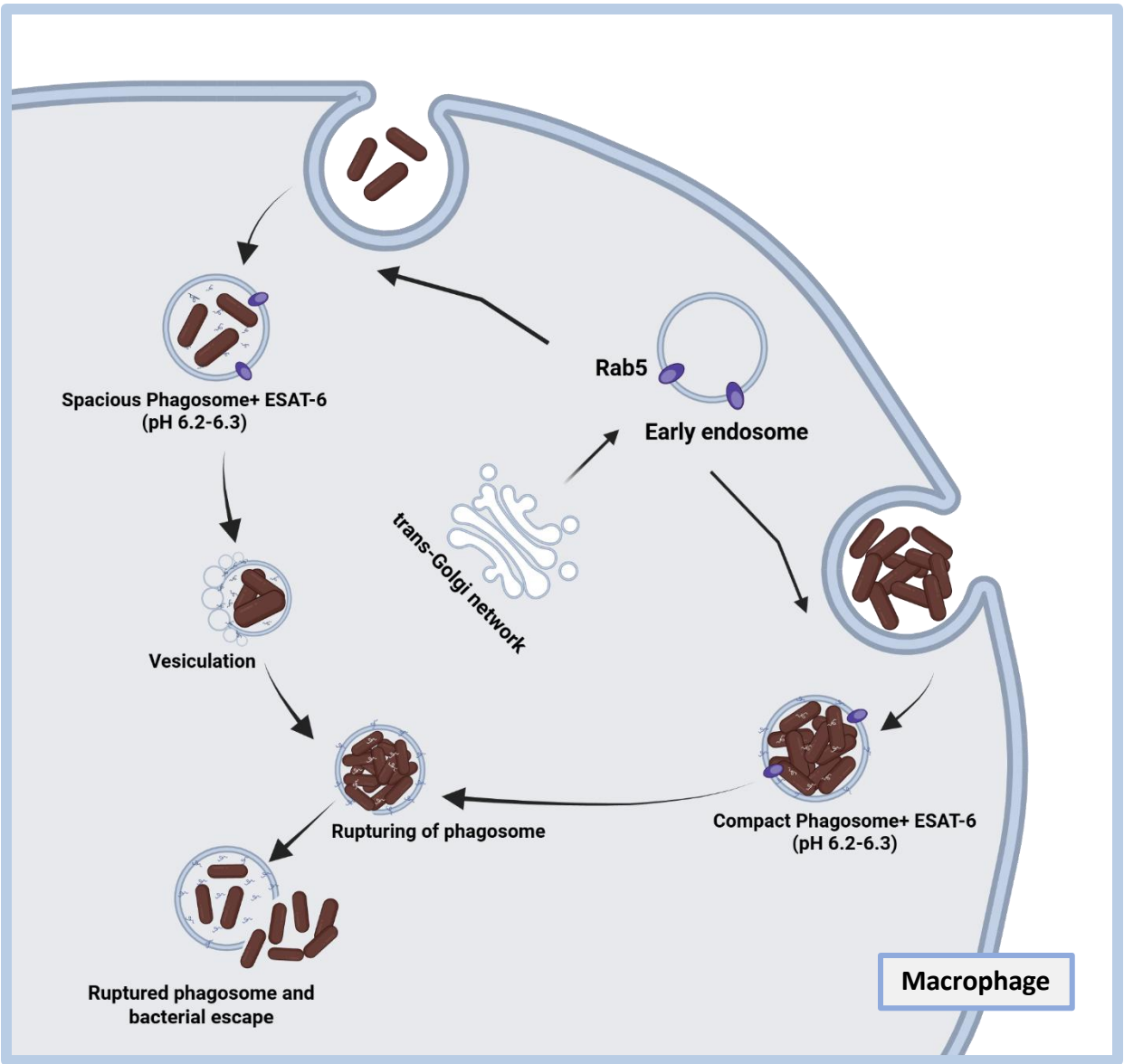
Spacious Phagosome+ ESAT-6
(pH 6.2-6.3)
Rab5
Early endosome
trans-Golgi network
Vesiculation
Rupturing of phagosome
Compact Phagosome+ ESAT-6
(pH 6.2-6.3)
Ruptured phagosome and
bacterial escape
Macrophage

Figure 6.

Schematic representation of the proposed mechanism of direct contact of mycobacteria enhances the virulence of ESAT-6

References

1. Cossart, P. & Sansonetti, P.J. Bacterial invasion: the paradigms of enteroinvasive pathogens. *Science (New York, N.Y.)* **304**, 242-248 (2004).
2. Case, E.D.R., Smith, J.A., Ficht, T.A., Samuel, J.E. & de Figueiredo, P.J.T. Space: a final frontier for vacuolar pathogens. **17**, 461-474 (2016).
3. Galán, J.E. & Collmer, A. Type III secretion machines: bacterial devices for protein delivery into host cells. *Science (New York, N.Y.)* **284**, 1322-1328 (1999).
4. Pizarro-Cerdá, J. & Cossart, P. Bacterial adhesion and entry into host cells. *Cell* **124**, 715-727 (2006).
5. Riethmüller, J., Riehle, A., Grassmé, H. & Gulbins, E. Membrane rafts in host-pathogen interactions. *Biochimica et biophysica acta* **1758**, 2139-2147 (2006).
6. Eierhoff, T. *et al.* A lipid zipper triggers bacterial invasion. **111**, 12895-12900 (2014).
7. Veiga, E. *et al.* Invasive and adherent bacterial pathogens co-Opt host clathrin for infection. *Cell host & microbe* **2**, 340-351 (2007).
8. Kühbacher, A. *et al.* Genome-Wide siRNA Screen Identifies Complementary Signaling Pathways Involved in Listeria Infection and Reveals Different Actin Nucleation Mechanisms during Listeria Cell Invasion and Actin Comet Tail Formation. *mBio* **6**, e00598-00515 (2015).
9. Pieters, J. Mycobacterium tuberculosis and the macrophage: maintaining a balance. *Cell host & microbe* **3**, 399-407 (2008).
10. Augenstreich, J. *et al.* The conical shape of DIM lipids promotes Mycobacterium tuberculosis infection of macrophages. *Proceedings of the National Academy of Sciences of the United States of America* **116**, 25649-25658 (2019).
11. Hagedorn, M., Rohde, K.H., Russell, D.G. & Soldati, T. Infection by tubercular mycobacteria is spread by nonlytic ejection from their amoeba hosts. *Science (New York, N.Y.)* **323**, 1729-1733 (2009).
12. Gerstenmaier, L. *et al.* The autophagic machinery ensures nonlytic transmission of mycobacteria. *Proceedings of the National Academy of Sciences of the United States of America* **112**, E687-692 (2015).
13. Simeone, R., Sayes, F., Lawarée, E. & Brosch, R. Breaching the phagosome, the case of the tuberculosis agent. *Cellular microbiology* **23**, e13344 (2021).
14. Russell, D.G. Who puts the tubercle in tuberculosis? *Nature reviews. Microbiology* **5**, 39-47 (2007).
15. Russell, D.G. Mycobacterium tuberculosis: here today, and here tomorrow. *Nature reviews. Molecular cell biology* **2**, 569-577 (2001).
16. Bussi, C. & Gutierrez, M.G. Mycobacterium tuberculosis infection of host cells in space and time. *FEMS microbiology reviews* **43**, 341-361 (2019).
17. Gröschel, M.I., Sayes, F., Simeone, R., Majlessi, L. & Brosch, R. ESX secretion systems: mycobacterial evolution to counter host immunity. *Nature reviews. Microbiology* **14**, 677-691 (2016).
18. van der Wel, N. *et al.* M. tuberculosis and M. leprae translocate from the phagolysosome to the cytosol in myeloid cells. *Cell* **129**, 1287-1298 (2007).
19. Houben, D. *et al.* ESX-1-mediated translocation to the cytosol controls virulence of mycobacteria. *Cellular microbiology* **14**, 1287-1298 (2012).
20. Simeone, R. *et al.* Phagosomal rupture by Mycobacterium tuberculosis results in toxicity and host cell death. *PLoS pathogens* **8**, e1002507 (2012).

21. De Leon, J. *et al.* Mycobacterium tuberculosis ESAT-6 exhibits a unique membrane-interacting activity that is not found in its ortholog from non-pathogenic Mycobacterium smegmatis. *The Journal of biological chemistry* **287**, 44184-44191 (2012).
22. Kennedy, G.M., Hooley, G.C., Champion, M.M., Mba Medie, F. & Champion, P.A. A novel ESX-1 locus reveals that surface-associated ESX-1 substrates mediate virulence in Mycobacterium marinum. *Journal of bacteriology* **196**, 1877-1888 (2014).
23. Raffetseder, J., Iakobachvili, N., Loitto, V., Peters, P.J. & Lerm, M. Retention of EsxA in the Capsule-Like Layer of Mycobacterium tuberculosis Is Associated with Cytotoxicity and Is Counteracted by Lung Surfactant. *Infection and immunity* **87** (2019).
24. Conrad, W.H. *et al.* Mycobacterial ESX-1 secretion system mediates host cell lysis through bacterium contact-dependent gross membrane disruptions. *Proceedings of the National Academy of Sciences of the United States of America* **114**, 1371-1376 (2017).
25. Lerner, T.R. *et al.* Phthiocerol dimycocerosates promote access to the cytosol and intracellular burden of Mycobacterium tuberculosis in lymphatic endothelial cells. *BMC biology* **16**, 1 (2018).
26. Cambier, C.J., Banik, S.M., Buonomo, J.A. & Bertozzi, C.R. Spreading of a mycobacterial cell-surface lipid into host epithelial membranes promotes infectivity. *eLife* **9** (2020).
27. Augenstreich, J. *et al.* ESX-1 and phthiocerol dimycocerosates of Mycobacterium tuberculosis act in concert to cause phagosomal rupture and host cell apoptosis. *Cellular microbiology* **19** (2017).
28. Barczak, A.K. *et al.* Systematic, multiparametric analysis of Mycobacterium tuberculosis intracellular infection offers insight into coordinated virulence. *PLoS pathogens* **13**, e1006363 (2017).
29. Astarie-Dequeker, C. *et al.* Phthiocerol dimycocerosates of M. tuberculosis participate in macrophage invasion by inducing changes in the organization of plasma membrane lipids. *PLoS pathogens* **5**, e1000289 (2009).
30. Sachdeva, K. *et al.* Mycobacterium tuberculosis (Mtb) lipid mediated lysosomal rewiring in infected macrophages modulates intracellular Mtb trafficking and survival. **295**, 9192-9210 (2020).
31. Lienard, J. *et al.* The Mycobacterium marinum ESX-1 system mediates phagosomal permeabilization and type I interferon production via separable mechanisms. *Proceedings of the National Academy of Sciences of the United States of America* **117**, 1160-1166 (2020).
32. Takatori, S.C. & Sahu, A. Active Contact Forces Drive Nonequilibrium Fluctuations in Membrane Vesicles. *Physical review letters* **124**, 158102 (2020).
33. Dai, S. *et al.* Lipid Giant Vesicles Engulf Living Bacteria Triggered by Minor Enhancement in Membrane Fluidity. *Nano letters* **23**, 371-379 (2023).
34. Le Nagard, L. *et al.* Encapsulated bacteria deform lipid vesicles into flagellated swimmers. *Proceedings of the National Academy of Sciences of the United States of America* **119**, e2206096119 (2022).
35. Behura, A. *et al.* ESAT-6 impedes IL-18 mediated phagosome lysosome fusion via microRNA-30a upon Calcimycin treatment in mycobacteria infected macrophages. Int Immunopharmacol **101**, 108319 (2021).
36. Wong, D., Bach, H., Sun, J., Hmama, Z. & Av-Gay, Y.J.P.o.t.N.A.o.S. Mycobacterium tuberculosis protein tyrosine phosphatase (PtpA) excludes host vacuolar-H+–ATPase to inhibit phagosome acidification. Proceedings of the National Academy of Sciences **108**, 19371-19376 (2011).
37. Sparks, I.L., Derbyshire, K.M., Jacobs, W.R., Jr. & Morita, Y.S. Mycobacterium smegmatis: The Vanguard of Mycobacterial Research. *Journal of bacteriology* **205**, e0033722 (2023).

38. Baumgart, T., Hunt, G., Farkas, E.R., Webb, W.W. & Feigenson, G.W. Fluorescence probe partitioning between Lo/Ld phases in lipid membranes. *Biochimica et biophysica acta* **1768**, 2182-2194 (2007).
39. Chakraborty, P., Bajeli, S., Kaushal, D., Radotra, B.D. & Kumar, A. Biofilm formation in the lung contributes to virulence and drug tolerance of Mycobacterium tuberculosis. *Nature communications* **12**, 1606 (2021).
40. Warner, D.F., Barczak, A.K., Gutierrez, M.G. & Mizrahi, V. Mycobacterium tuberculosis biology, pathogenicity and interaction with the host. *Nature reviews. Microbiology* (2025).
41. Van der Ham, S., Agudo-Canalejo, J. & Vutukuri, H.R.J.A.n. Role of shape in particle-lipid membrane interactions: from surfing to full engulfment. **18**, 10407-10416 (2024).
42. Barisch, C., Paschke, P., Hagedorn, M., Maniak, M. & Soldati, T.J.C.m. Lipid droplet dynamics at early stages of M ycobacterium marinum infection in Dictyostelium. Cellular microbiology **17**, 1332-1349 (2015).
43. Rohde, K.H., Veiga, D.F., Caldwell, S., Balázsi, G. & Russell, D.G.J.P.p. Linking the transcriptional profiles and the physiological states of Mycobacterium tuberculosis during an extended intracellular infection.PLoS pathogens **8**, e1002769 (2012).
44. Schnettger, L. *et al.* A Rab20-dependent membrane trafficking pathway controls M. tuberculosis replication by regulating phagosome spaciousness and integrity. Cell host microbe **21**, 619-628. e615 (2017).
45. Pandey, A.K. & Sassetti, C.M. Mycobacterial persistence requires the utilization of host cholesterol. *Proceedings of the National Academy of Sciences of the United States of America* **105**, 4376-4380 (2008).
46. Vincent, O., Sreekumari, A., Gopalakrishnan, M., Vasisht, V.V. & Sarangi, B.R.J.P.R.E. Curvature-dependent dynamics of a bacterium confined in a giant unilamellar vesicle. **112**, 024408 (2025).
47. Veatch, S.L. *et al.* Critical fluctuations in plasma membrane vesicles. *ACS chemical biology* **3**, 287-293 (2008).
48. Burns, M., Wisser, K., Wu, J., Levental, I. & Veatch, S.L. Miscibility Transition Temperature Scales with Growth Temperature in a Zebrafish Cell Line. *Biophysical journal* **113**, 1212-1222 (2017).
49. Gray, E., Karslake, J., Machta, B.B. & Veatch, S.L. Liquid general anesthetics lower critical temperatures in plasma membrane vesicles. *Biophysical journal* **105**, 2751-2759 (2013).
50. Gray, E.M., Díaz-Vázquez, G. & Veatch, S.L. Growth Conditions and Cell Cycle Phase Modulate Phase Transition Temperatures in RBL-2H3 Derived Plasma Membrane Vesicles. *PloS one* **10**, e0137741 (2015).
51. Rouches, M., Veatch, S.L. & Machta, B.B. Surface densities prewet a near-critical membrane. *Proceedings of the National Academy of Sciences of the United States of America* **118** (2021).
52. Sorre, B. *et al.* Curvature-driven lipid sorting needs proximity to a demixing point and is aided by proteins. **106**, 5622-5626 (2009).
53. Vutukuri, H.R. *et al.* Active particles induce large shape deformations in giant lipid vesicles. *Nature* **586**, 52-56 (2020).
54. Koiri, D. *et al.* Real-time visualization reveals Mycobacterium tuberculosis ESAT-6 disrupts phagosome-like compartment via fibril-mediated vesiculation. Cell reports **44** (2025).
55. Bosmani, C. *et al.* Membrane microdomains are crucial for Mycobacterium marinum EsxA-dependent membrane damage, escape to the cytosol and infection. BioRxiv2024.2008.2019.608731 (2024).

56. Kulakowski, G. *et al.* Lipid packing defects and membrane charge control RAB GTPase recruitment. *Traffic (Copenhagen, Denmark)* **19**, 536-545 (2018).
57. Saleem, M. *et al.* A balance between membrane elasticity and polymerization energy sets the shape of spherical clathrin coats. *Nature communications* **6**, 6249 (2015).
58. Kaksonen, M. & Roux, A. Mechanisms of clathrin-mediated endocytosis. *Nature reviews. Molecular cell biology* **19**, 313-326 (2018).
59. Larsen, J.B. *et al.* Membrane curvature enables N-Ras lipid anchor sorting to liquid-ordered membrane phases. *Nature chemical biology* **11**, 192-194 (2015).
60. Prince, A. *et al.* Lipid Specificity of the Fusion of Bacterial Extracellular Vesicles with the Host Membrane. *The journal of physical chemistry. B* **128**, 8116-8130 (2024).
61. Morlot, S. *et al.* Membrane shape at the edge of the dynamin helix sets location and duration of the fission reaction. *Cell* **151**, 619-629 (2012).
62. Evans, E. & Rawicz, W. Entropy-driven tension and bending elasticity in condensed-fluid membranes. *Physical review letters* **64**, 2094-2097 (1990).
63. Kwok, R. & Evans, E. Thermoelasticity of large lecithin bilayer vesicles. *Biophysical journal* **35**, 637-652 (1981).
64. Rawicz, W., Olbrich, K.C., McIntosh, T., Needham, D. & Evans, E. Effect of chain length and unsaturation on elasticity of lipid bilayers. *Biophysical journal* **79**, 328-339 (2000).
65. Sundaramurthy, V. *et al.* Deducing the mechanism of action of compounds identified in phenotypic screens by integrating their multiparametric profiles with a reference genetic screen. *Nature protocols* **9**, 474-490 (2014).
66. Sundaramurthy, V. *et al.* Survival of Mycobacterium tuberculosis and Mycobacterium bovis BCG in lysosomes in vivo. Nature Protocols **19**, 515-526 (2017).

Acknowledgements

We thank Rohan Dhiman for the kind gift of the ESAT-6 plasmid and GFP-*M. smegmatis* strain. We thank Shubhay Arvind Dikkar and Sajag Kumar for their inputs during technical discussion. We also thank Abik Hameem P.M. and Dipam Naskar for their initial help with micropipette experiments. We acknowledge all the members of the M.S. lab for critical reading of the manuscript. We thank the Biosafety and Central Imaging and Flow Cytometry (CIFF) facilities at NCBS. SC is supported by the Ramalingaswami Re-entry Fellowship (BT/HRD/35/02/2006), Ministry of Science and technology, Government of India. MS gratefully acknowledges the DBT-Wellcome Trust India Alliance (Grant- IA/I/20/2/505212) and Department of Atomic Energy for financial support. VS acknowledges core funding from NCBS-TIFR and Department of Atomic Energy.